Structural anisotropy of normal fault surfaces

JOONG-JEEK LEE* and RONALD L. BRUHN

Department of Geology and Geophysics, University of Utah, Salt Lake City, UT 84112, U.S.A.

Abstract—Precise description of natural fault surfaces is indispensable to understanding the geometry, mechanics and fluid transport properties of faults. Profiles of fault surfaces in the Wasatch fault zone and Oquirrh Mountains, Utah, are measured at 30° increments within the fault plane to determine the directional anisotropy of surface roughness at wavelengths between 10^{-3} m and 30 m, and then compared with profiles of larger-scale fault surfaces. Surface anisotropy and an increasing ratio of surface amplitude to wavelength are consistent with self-affine fault topography at wavelengths between 1 mm and approximately 5 km. Fractal dimension of surface profiles generally decreases systematically as the angle to the slip direction increases. Directional anisotropy is described by an azimuthal scaling function $\gamma_\phi = K \sin(\phi) + \gamma_0$ or $AF_\phi = (AF_{max} - 1)\sin(\phi) + 1$, where γ_ϕ and AF_ϕ are the amplitude to wavelength ratio and anisotropy factor respectively at azimuth ϕ, measured clockwise relative to slip direction within the fault surface, and γ_0 is the amplitude to wavelength ratio parallel to slip direction. $K = (\gamma_{90} - \gamma_0)$ is an anisotropy coefficient and increases systematically with spatial wavelength on the fault surface. Characterization of natural fault surfaces provides parameters such as fractal dimension (D), intercept ($\log(C)$) of power spectra, profile variance, and variation in anisotropy factor (AF), which are needed to generate fractal models of natural fault surfaces using spectral synthesis. We generate sample models which illustrate the differences between fault surfaces characterized by constant versus azimuthally varying fractal dimension. The latter model surfaces contain low amplitude corrugations superimposed on elongate ridges which parallel slip direction. This surface texture resembles that of natural fault surfaces that refract across lithologic layering or are cut by secondary faults such as R and R' shears. Copyright © 1996 Elsevier Science Ltd

INTRODUCTION

Describing and predicting the geometry of natural rock fracture surfaces is important because surface roughness affects the mechanical and hydraulic behavior of joints and faults. Anderson (1951) recognized that faults are not planar, but irregular on all scales with strong spatial anisotropy. Fault surfaces contain non-cylindrical ridges and furrows, or corrugations elongated parallel to slip direction (Power *et al.* 1987, 1988, Scholz 1990, pp. 145–147). There are two basic approaches to the description of surface roughness, Euclidean and fractal measures (Power & Tullis 1991). Euclidean measures include statistical descriptions such as root mean square roughness (σ_{rms}) and centerline average roughness (R_a). Fractal measures characterize roughness by the fractal dimension (D), which is a parameter describing the scaling properties of surface topography. Fractal measures are widely used in the characterization of natural objects and processes that are irregular and chaotic (Mandelbrot 1967, 1983). Several authors conclude that the roughness of natural faults and fractures is fractal (Brown & Scholz 1985, Brown *et al.* 1986, Scholz & Aviles 1986, Power *et al.* 1987, 1988, Power & Tullis 1991, Power & Tullis 1992). Fractal measures of rock surface roughness are applied to estimate the strength and stiffness of rock joints (Barton 1986, Brown & Scholz 1986), fluid flow through fractures (Brown 1987, Wang *et al.* 1988, Nolte

et al. 1989), wear processes during fault zone evolution (Scholz 1987, Power *et al.* 1988, Power & Tullis 1992), and surface properties of earthquake rupture (Aviles *et al.* 1987, Okubo & Aki 1987, Bruhn *et al.* 1991).

We surveyed several fault surfaces in the Salt Lake and Provo segments of the Wasatch fault zone, and in the western part of the southern Oquirrh Mountains, Utah, U.S.A., to investigate the scaling properties and anisotropy of fault surfaces. We apply fractal measures to fault surfaces at distances between 10^{-3} m and 30 m to characterize directional anisotropy and to define a scaling law that predicts roughness as a function of both distance and direction along fault surfaces. The results are extrapolated to larger scale using data from fault-controlled ore deposits in underground mines. We also discuss possible reasons for the observed change in scaling properties at various wavelengths. Finally, we generate sample fractal models of natural fault surfaces based on scaling parameters determined from the field measurements.

GEOLOGIC SETTING

Wasatch fault zone

The Wasatch normal fault zone forms part of the eastern boundary of the Basin and Range province in the western United States. The fault zone extends approximately 370 km from southern Idaho to central Utah (Machette *et al.* 1987, 1991, Schwartz & Coppersmith 1984). The Wasatch fault zone is divided into 10 segments

---

* Corresponding address: Department of Geology and Geophysics, University of Utah, Salt Lake City, Utah 84112, U.S.A. E-mail: leejoong@mines.utah.edu or rlbruhn@mines.utah.edu.

based on the geometry of the fault zone and evidence for the time of recent fault movements (Machette *et al.* 1991). The Salt Lake and Provo segment are two of these 10 segments. We measured fault surfaces at three sites in the Wasatch fault zone; two in the Salt Lake segment (Red Butte and Draper) and one in the Provo segment (Seven Peaks) (Fig. 1). The Red Butte site is located in Mesozoic and Paleozoic strata in the northern part of the Salt Lake segment. The Draper site is located at the southern end of the Salt Lake segment in Precambrian metamorphic rocks and Tertiary quartz monzonite of the Little Cottonwood stock. The Seven Peak site is located in Paleozoic strata in the central part of the Provo segment.

The fault surface measured at the Red Butte site cuts through Triassic limestone with thin shale interbeds, and is one of many subsidiary normal faults developed in a band 1–2 km wide that parallels the Quaternary trace of the Wasatch fault zone in the Salt Lake segment (Gibler 1985, Bruhn *et al.* 1987). The time of faulting is not well constrained, but the location and paleo-stress directions inferred from fault kinematics indicates that faulting occurred under the Late Tertiary extensional stress regime (Gibler 1985). The Red Butte fault surface strikes N10°W to N15°W, dips 32°W to 38°W, and contains grooves trending 320°–330°.

Several fault surfaces were measured at the Draper site. These faults cut white to rusty brown weathering quartzite of the Upper Proterozoic Big Cottonwood Formation. The faults form triangular facets that Gilbert (1928) interpreted to be part of the exhumed Wasatch fault zone. In detail, there are several parallel faults that give the quartzite a crude, sheet-like structure parallel to the faces of the triangular facets. The faults strike N10°W to N30°E, dip 35°W to 50°W, and contain slickenlines and grooves trending 230° to 290°.

The fault surface measured at the Seven Peak site cuts Mississippian limestone. The surface is exhumed because Quaternary gravel was excavated from the bedrock. The excavated surface is ~ 900 m^2, allowing measurement of surface profiles up to 30 m in length. The last faulting event occurred during the Holocene (Machette *et al.* 1991). The Seven Peak surface strikes N10°E to N20°E, dips 40°W to 45°W, and contains slickenlines and grooves trending 235°–260°.

Oquirrh Mountains

The Oquirrh Mountains are located about 30 km west of Salt Lake City in the eastern part of the Great Basin (Fig. 1). The Soldier Canyon site is located in the north central part of the Soldier Canyon fault zone, a zone of normal faulting developed in Upper Mississippian limestone along the western flank of the mountain range. Although the age of the most recent faulting is uncertain, it is probably late Quaternary based on the degree of
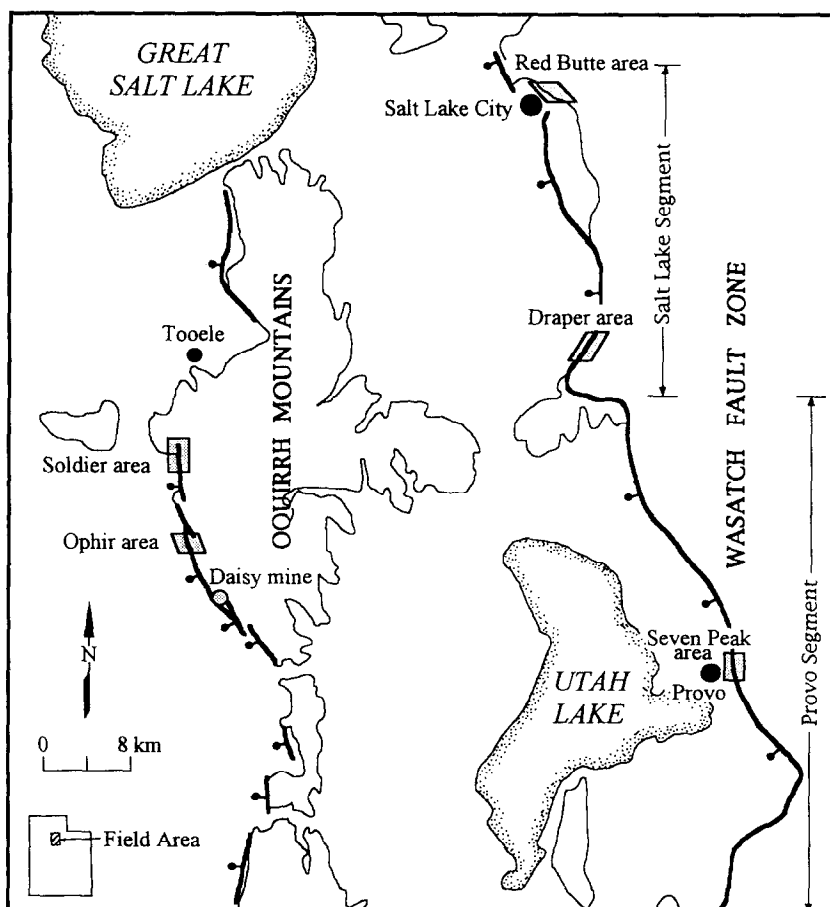

Fig. 1. Index map of study areas in the Wasatch fault zone and the southern Oquirrh Mountains, Utah, U.S.A.

weathering of the fault surface and the age of adjacent scarps in unconsolidated deposits (Wu & Bruhn 1994). The fault surface strikes N20°W, dips 50°SW, and the slip direction trends 245°–250°.

The Ophir Canyon site is located in Upper Mississippian limestone at the northern end of the West Mercur fault zone, a zone of Late Tertiary normal faults. The Ophir fault surface strikes N20°E, dips 70°NW, and the slip direction trends 280°–290°.

DATA COLLECTION AND ANALYSIS

Data collection

Profiles on fault surfaces were made in the field using two types of stylus profilometer: one a digital stylus, and the other a sliding pin contour gauge. A tape measure was used for profiles longer than 1.2 m. The digital stylus profilometer was used to measure profiles of fault surfaces at scales between 1 mm and 1.2 m with a sampling interval of 0.5 mm. The device consists of an aluminum rail and sliding stylus. Horizontal and vertical potentiometers record the position of the stylus on a portable data logger. The sliding pin contour gauge was used to measure 15 cm length profiles with a sampling interval of 0.7 mm. A stretched tape measurement was used for profiles at scales between 1 m and 30 m with a sampling interval of 2–5 cm. The longest and shortest wavelengths in the data sets were the profile length and twice the sampling interval or Nyquist cutoff wavelength, respectively. The sampling interval was smaller than the cutoff wavelength for the stylus profilometer in order to avoid aliasing of short wavelengths. The digital stylus had mechanical measurement errors of ±0.4 mm over a vertical displacement range of 85.0 mm. The horizontal displacement error was ±0.6 mm over the maximum range of 1215 mm. The horizontal precision error was less than the instrumental detection limits of 0.5 mm, but the vertical precision error of ±1.0 mm was about twice as large as the vertical mechanical error, mostly due to binding of the vertical potentiometer during sliding over rough surfaces.

Power *et al.* (1987) found that the amplitude to wavelength ratio of fault surface topography changed when measured parallel and perpendicular to fault slip direction. In this study, we extend the type of measurements made by Power *et al.* (1987) to include profiles at several azimuths between the slip-parallel and slip-perpendicular directions. We have investigated scaling between amplitude and wavelength by measuring profiles at azimuthal increments of 30° within the fault surfaces (Fig. 2). The measurements were repeated at two to four different sites on the fault surface. Three to four parallel profiles were measured at each azimuth at every site, in order to obtain representative profiles of the surface and to aid data processing during power spectra computation. Profiles between 10^2 m and 10^4 m long were obtained by digitizing mapped fault surfaces from an

underground mine (Daisy Mine) in the Oquirrh fault zone, and fault traces from published maps of the Salt Lake segment in the Wasatch fault zone (Crittenden 1965, Hintze 1978, Horn & Crittenden 1987, Wu & Bruhn 1994). These profiles represent large scale, averaged fault topography that can then be compared with the shorter profiles measured on outcrops in the same fault zone. The digitized, map scale fault traces were rotated to a down-dip view before data analysis in order to remove topographic effects on fault trace sinuosity. The sinuosity or true amplitude of the mapped fault traces was found as follows: we digitized the fault traces, found the average strike and dip of the fault by fitting a plane through the traces using linear, least-squares regression, and then rotated the data points so the best fit plane dips 90°. The resulting profile is the deviation of the fault trace about the best fit plane.

Fourier power spectral method

Surface roughness is described by the Fourier power spectral method (Brown & Scholz 1985, Power *et al.* 1987, 1988, Power & Tullis 1991). A power spectrum from each profile is computed using a fast Fourier transform (FFT) algorithm, following the recommendation of Bendat & Piersol (1986) as described in Brown & Scholz (1985) and Power *et al.* (1988). The steps in the procedure are as follows. 1) Removal of linear trend from the profile data. 2) Cosine tapering of the first and last 10% of the data points to diminish "leaking" of power at each side of the spectrum caused by finite profile length. 3) Calculation of spectral amplitudes using a fast Fourier transform (FFT) program. A raw estimate of power spectral density is calculated by squaring the amplitude at each frequency. 4) The raw power spectra are normalized by dividing the power at each frequency by the length of the profile. 5) Spectra from each of the 3 or 4 parallel profiles measured along a specific azimuth at each site are averaged to produce a smooth spectrum and reduce spurious variations introduced in single profile spectra because of the discrete frequency resolution of the FFT (Brown & Scholz 1985, Power *et al.* 1988). 6) A Hanning filter is applied to the averaged power spectra to smooth the curve and improve estimation of the power spectral density. 7) Parts of profiles collected with the different instruments (contour gauge, digital stylus, or tape measure) are joined together where the frequency range of each instrument overlaps. Linear least squares regression is then used to compute the slope (a) and intercept (log(*C*)) for each average profile. In most cases the profiles can be visually segmented into linear sections with different slope. In these cases, linear regression is carried out on each segment separately. This procedure is repeated for each of the six reference directions on the fault surface.

Fractal surfaces are characterized by a power spectral density function $G(f)$ of the form:

$$G(f) = Cf^{-\alpha} \qquad (1)$$

(a)

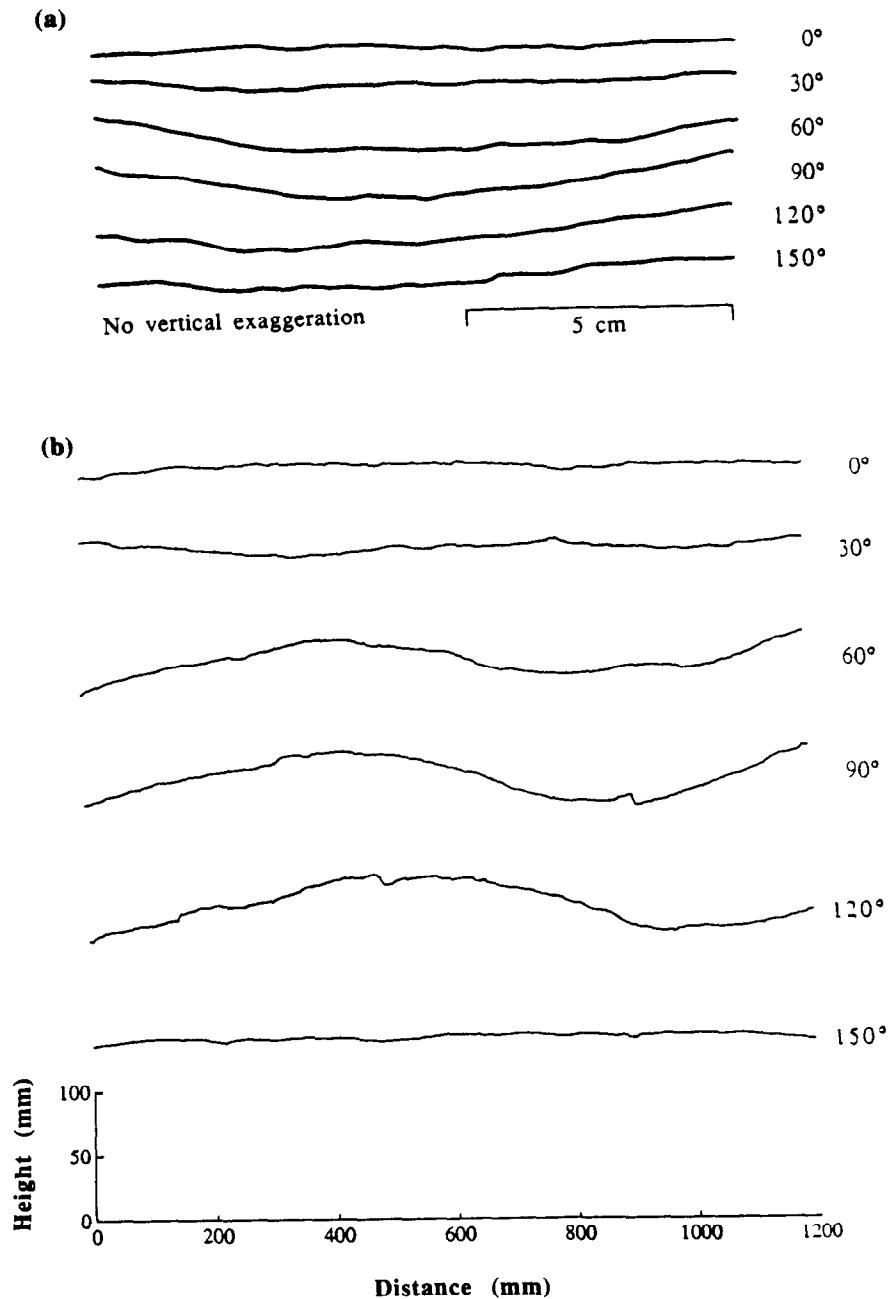No vertical exaggeration

(b)

Fig. 2. Examples of fault surface profiles. The number on the right side is the azimuth of the profile measured clockwise with respect to slip direction as viewed down-dip. Note that the profiles change significantly as the azimuth varies. (a) Example of surface profiles of a fault measured with a contour gauge. (b) Example of surface profiles of a fault measured with a digital stylus.

or:

$$\log\{G(f)\} = \log(C) - \alpha\log(f)$$

where f is the spatial frequency and C is a constant (Berry & Lewis 1980, Brown & Scholz 1985, Scholz & Aviles 1986, Power & Tullis 1991). Least squares regression of $\log\{G(f)\}$ versus $\log(f)$ determines the slope ($-\alpha$) and intercept, $\log(C)$, of the power spectrum (Fig. 3). α determines how the surface topography changes or 'scales' with wavelength. Log(C), together with α, describes the steepness of the surface topography or total profile variance (mean square amplitude) at a specific wavelength (Power & Tullis 1991). Berry &

Lewis (1980) derived the relationship between the slope of power spectra (α) and fractal dimension (D) as

$$D = 2.5 - \alpha/2 (2 \le \alpha \le 3) \tag{2}$$

corresponding to $1.0 \le D \le 1.5$, where $D = 1.5$, this corresponds to fractional Brownian profile. Large D implies smaller slope (α), so there is greater amplitude at shorter wavelength relative to a longer wavelength than if D is small. The profile becomes more jagged or rough appearing as D increases. Fractal dimension (D) is a measure of amplitude or scaling as a function of wavelength, but does not by itself provide information about the amplitude. Computing the amplitude at a
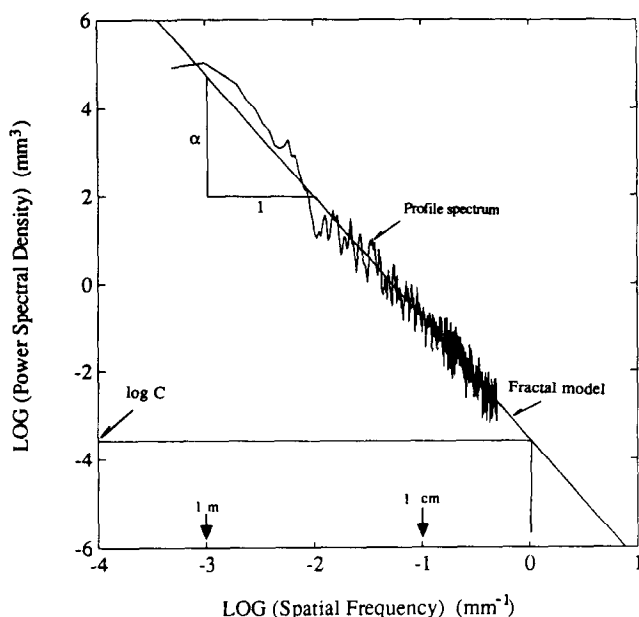
LOG (Spatial Frequency) (mm⁻¹)

Fig. 3. The determination and description of a fractal profile model by the spectral method. Estimates of power spectral density are described by a line of slope (α) and intercept ($\log(C)$) using a linear fractal model (solid line). The slope (α) determines scaling properties of amplitude versus wavelength, and the intercept ($\log(C)$) determines the magnitude of the surface elevation for a given slope (α) (after Power & Tullis 1991).

specific wavelength also requires the intercept coefficient '$\log(C)$'.

Amplitude to wavelength ratio from power spectra and the scaling law

Power spectra describe the distribution of amplitude at various wavelengths within a fault profile (Power *et al.* 1987, 1988, Power & Tullis 1991). The dimensionless

amplitude to wavelength ratio (γ) is used to visualize the results of spectral analyses, following the treatment presented by Kamb (1970) and Power & Tullis (1991). We need to consider a case in which the amplitude to wavelength ratio (γ) scales with wavelength, because natural fault surfaces are self-affine and γ decreases with increasing wavelength.

The root mean square variance (σ_{rms}) of fault surfaces increases approximately linearly as the profile length is increased. σ_{rms} may be compared with power spectra because it is equal to the square root of the area under the power spectral density function $G(f)$ (Power *et al.* 1988, Power & Tullis 1991).

$$\sigma_{rms} = \left\{ \int_{f_{min}}^{f_{max}} G(f) df \right\}^{1/2} \qquad (3)$$

where f_{min} and f_{max} are the lowest and highest frequencies considered, respectively. The lowest frequency (f_{min}) is equal to $1/L$ where L is the profile length. We consider the changing amplitude to wavelength ratio for a profile with a geometric frequency sequence, where the frequency change is a multiple of 2. The distance between each discrete frequency in the geometric sequence is variable when plotted on an arithmetic scale or graph (Fig. 4, left), but this distance is constant when plotted on a logarithmic scale (Fig. 4, right). On a logarithmic scale, each frequency has a center frequency $f_k = 2^{(k-1)} f_{min}$ with interval Δf (Fig. 4, right), where

$$\Delta f = \sqrt{2} f_k - \frac{f_k}{\sqrt{2}} = \frac{f_k}{\sqrt{2}} \qquad (4)$$

on the logarithmic axis.

The profile variance within the frequency interval results from substituting (1) into (3) with (4) and
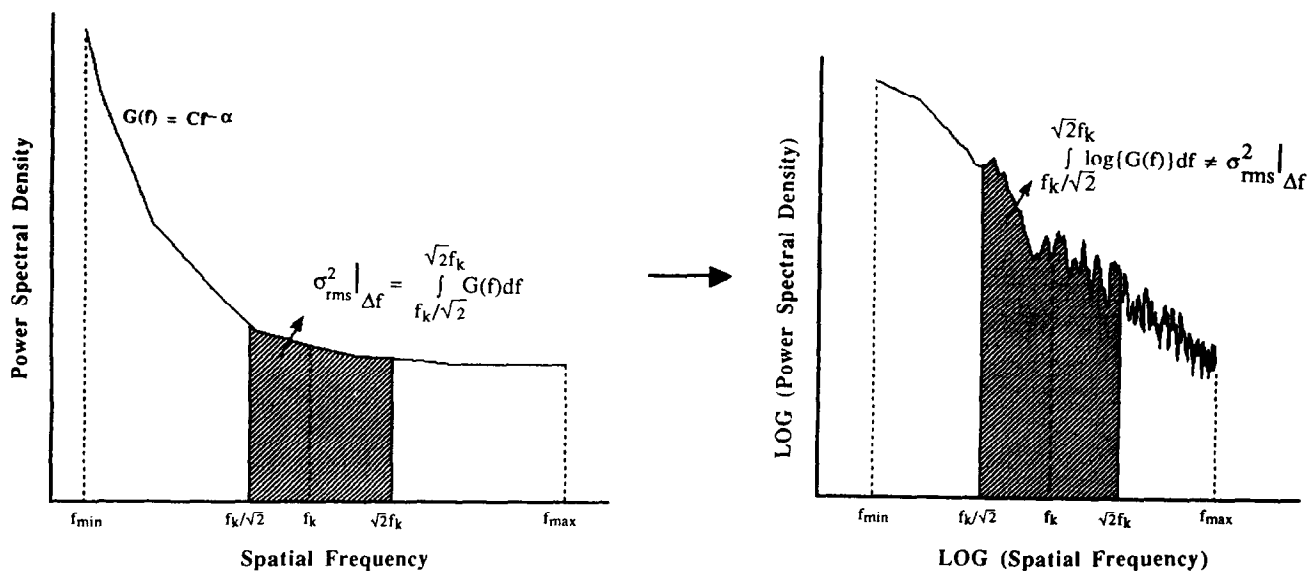

Spatial Frequency

LOG (Spatial Frequency)

Fig. 4. Characteristics of the root mean square variance (σ^2_{rms}) and the total power within a geometric frequency interval (Δf) at a given center frequency (f_k) using the relationship between the amplitude to wavelength ratio (γ_k) and slope (α) and intercept ($\log(C)$) of the power spectrum. σ^2_{rms} is equal to the area under the power spectral density function ($G(f)$) and can be decided by γ_k on an arithmetic scale (left). It is, however, controlled by α and $\log(C)$ of power spectrum on a logarithmic scale (right). Detailed derivation of the relationship is discussed in the text.

integrating to give:

$$\sigma_{rms}^2|_{\Delta f} = \int_{f_k/\sqrt{2}}^{\sqrt{2}f_k} G(f)df = \frac{C}{\alpha - 1}(f_k)^{1-\alpha}\left(\sqrt{2}^{\alpha-1} - \sqrt{2}^{1-\alpha}\right).$$

(5)

The profile variance within the specified frequency interval (Δf) can be compared with the mean square amplitude of a single sine wave with wavelength $\lambda_k = 1/f_k$ and amplitude $a_k = \gamma_k\lambda_k$. The mean square value of the sine wave is:

$$\sigma_{rms}^2|_{\Delta f} = \frac{a_k^2}{2} = \frac{\gamma_k^2\lambda_k^2}{2} = \frac{\gamma_k^2}{2f_k^2}$$

(6)

The relationship between γ_k, α, C, and f_k is found by combining (5) with (6):

$$\gamma_k^2 = \frac{2C}{\alpha - 1}(f_k)^{3-\alpha}\left(\sqrt{2}^{\alpha-1} - \sqrt{2}^{1-\alpha}\right)$$

(7)

or:

$$a_k^2 = \frac{2C}{\alpha - 1}(f_k)^{1-\alpha}\left(\sqrt{2}^{\alpha-1} - \sqrt{2}^{1-\alpha}\right).$$

For a self-similar profile generated by a geometric frequency sequence the slope (α) = 3, and the amplitude to wavelength ratio (γ_k) is independent of frequency, with the constant value

$$\gamma_k = \left(\frac{3}{2}C\right)^{1/2}.$$

(8)

In general, γ_k decreases with increasing wavelength for a geometric frequency sequence. However, if $\alpha_k = 3$, the profile generated by a geometric frequency sequence is self-similar, and γ_k is constant (equation 8).

Is the profile model of geometric frequency sequences most applicable to natural fault surfaces which are approximately 'Fractional Brownian' in surface topography? The answer may be found by comparing γ_k determined from spectral analysis with the relationship between mean elevation change (V) and spatial distance or wavelength (X) in the fundamental scaling law for self-affine fractional Brownian motion or displacement (Voss 1988):

$$V^2 = BX^{2H}$$

(9)

where H is the Hurst exponent, and is related to the fractal dimension D by $H = 2 - D$. In two-dimensions D may vary from 1.0 to 2.0 and H is constrained to $0 \le H \le 1.0$. D is estimated from the slope (α) of the power spectra using equation (9), $D = 2.5-\alpha/2$. The mean elevation change to wavelength ratio (δ) is found by dividing equation (12) by X^2 and taking the square root to give

$$\delta = \sqrt{B}X^{(H-1)}.$$

(10)

A normalized mean elevation change to wavelength ratio δ_{fBm} by reference to the self-similar case (δ_s), in which $H = 1.0$, $D = 1.0$, $\alpha = 3.0$ and $\delta_s = \sqrt{B}$, is defined as follows:

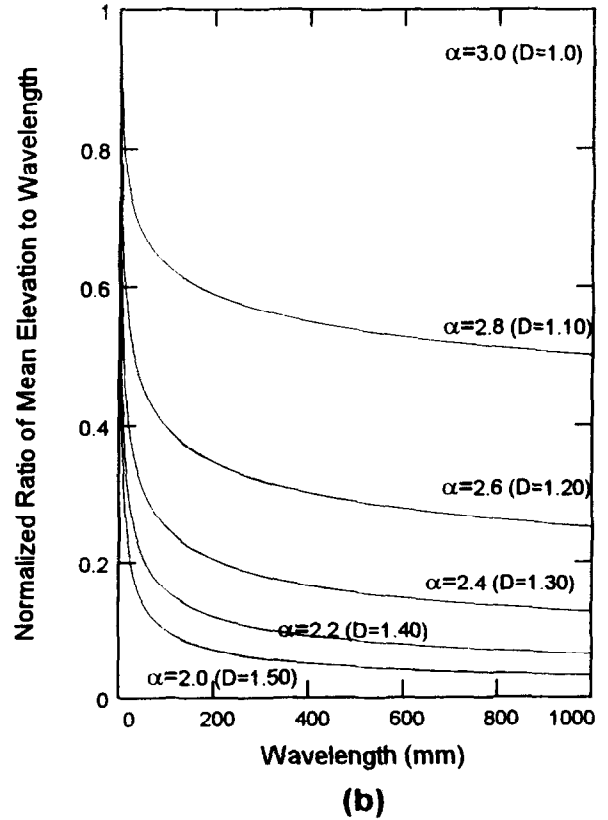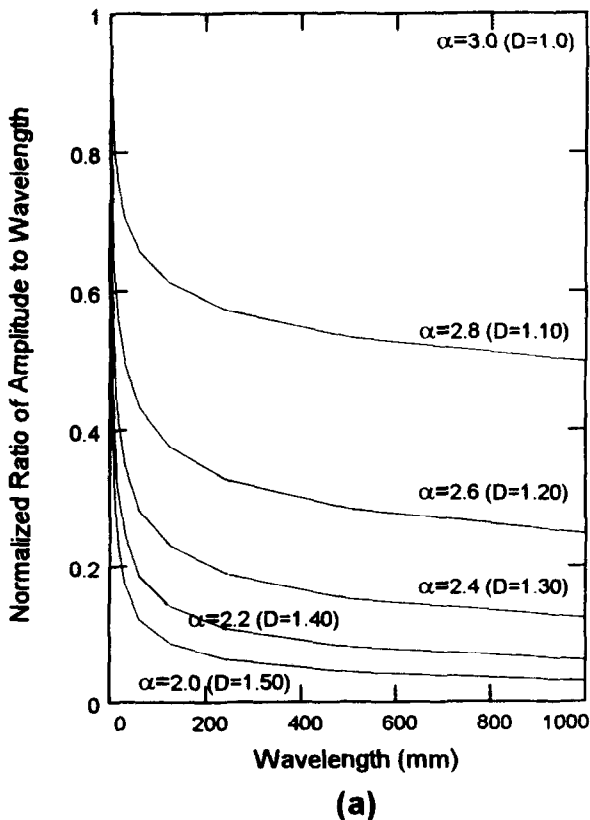$$\delta_{fBm} = [\delta/\delta_s] = X^{(H-1)}.$$

(11)

Fig. 5. Normalized ratio of amplitude to wavelength from power spectra and normalized ratio of mean elevation to wavelength from basic scaling law for fractal geometry. (a) Geometric frequency sequence. (b) Scaling law.

δ_{fBm} is compared to γ_k for profiles generated by the summation of geometric frequency sequences in Fig. 5. We conclude that the spectral analysis of fault profiles is best accomplished using the geometrical sequence model, in which γ_k decreases with increasing wavelength. We now apply these results to modeling the roughness and anisotropy of fault surfaces.

RESULTS

Variation of slopes and intercepts

The fault surface profiles of Fig. 2 show a strong direction dependent roughness or topography with respect to the slip direction, which is reflected in their ensembled power spectra (Fig. 6). Neither the slopes nor the intercepts of the power spectra are constant for profiles from the same fault surfaces (Figs. 6 and 7). Individual spectra can be also divided into segments of slope based on visual inspection of the logarithmic plot of power spectral density versus spatial frequency (Fig. 6). Slope, α, varies systematically with respect to fault slip direction for most profiles that are up to 15 cm long, obtaining maximum values in the direction perpendicular to slip and minimum values parallel to slip (Fig. 7a). Profiles perpendicular to slip direction have the greatest amplitude at a specific wavelength, and amplitude generally decreases as the profile azimuth approaches the slip-parallel direction. Slopes of power spectra at wavelengths between 1 mm and 15 cm are $\alpha = 1.94 \pm 0.05$ to $\alpha = 2.28 \pm 0.04$, which imply that the surface profiles are self-affine and the fractal dimension (D) is between 1.36 ± 0.02 and 1.53 ± 0.03; the latter value is close to 'Brownian motion' ($D = 1.5$). The average intercepts of power spectra range from $\log(C) = -3.08 \pm 0.02$ to $\log(C) = -3.04 \pm 0.03$. The surfaces are anisotropic because D is a function of profile azimuth.

At profile lengths between 15 cm and 1 m, the slopes of power spectra also generally increase as the profile azimuth varies between the slip direction and the direction perpendicular to slip (Fig. 7b), with the exception of the Soldier Canyon fault surface. Slopes range between $\alpha = 2.48 \pm 0.05$ and $\alpha = 2.75 \pm 0.04$, corresponding to $D = 1.13 \pm 0.02$ to $D = 1.26 \pm 0.03$. However, the intercepts of the power spectra do not vary systematically for all surfaces as the profile azimuth varies. They either fluctuate about a mean value of ≈ -3.30 to -3.70 (Fig. 7b, Draper fault surface) or decrease systematically as the azimuth increases (Seven Peak fault surface). The maximum observed change in the intercept ($\log(C)$) is ≈ -1.0 for the fault surface at the Seven Peak locality in the Wasatch fault zone. Azimuthal variations in the slope and intercept of power spectra from profiles longer than 1 m are similar to those from profiles between 15 cm and 1 m long. The magnitude of the slope and intercept is similar in the slip parallel direction, but significantly greater in the direction perpendicular to slip than predicted by extrapolation of data from the 15 cm to 1 m long profiles. The average slope in the direction perpen-

dicular to slip is $\alpha = 2.88 \pm 0.05$ while the intercept $\log(C) = -3.32 \pm 0.16$.

There is a significant change in slope and intercept of the power spectra located in the wavelength band between 5 cm and 15 cm (spatial frequency range between 10^{-1} and 10^{-2} mm^{-1}) (Fig. 8). The slope is greater and the intercept is less at wavelengths above 15 cm than at shorter wavelengths. This wavelength dependent property of the slope persists regardless of azimuth. However, the intercept remains essentially constant at all profile azimuths at wavelengths less than 15 cm, but either fluctuates or decreases systematically as a function of ϕ at longer wavelengths. A similar change in slope and intercept was noted in the same wavelength band by Power & Tullis (1991), and they ascribed this variation to weathering (pitting?) of the fault surface at short wavelengths. An alternative presented in the discussion is an increase in roughness at short wavelengths created by the drag of wear fragments along the fault surface during sliding, and secondary fracturing that roughens the fault surface.

Azimuthal scaling function and anisotropy

The directional anisotropy of surface roughness is evident by changes in both α and $\log(C)$ between profiles oriented at different azimuths with respect to slip direction (Fig. 7). There is no clear, systematic change in the slope and intercept of the power spectra, but both parameters change in such a way that within each of the three profile length intervals (1 mm $< \lambda <$ 15 cm, 15 cm $< \lambda <$ 1 m, $\lambda >$ 1 m) the amplitude to wavelength ratios $\gamma_\phi(\lambda)$ change systematically with respect to slip direction (Fig. 9). The azimuthal scaling function for γ_ϕ at the longest wavelength or lowest frequency in each of the specified profile length intervals is defined as:

$$\gamma_\phi = K\sin(\phi) + \gamma_0 \qquad (12)$$

or:

$$AF_\phi = (AF_{max} - 1)\sin(\phi) + 1$$

where $K = (\gamma_{90} - \gamma_0)$ is the anisotropy coefficient, γ_0 is the amplitude to wavelength ratio parallel to slip direction, γ_ϕ and AF_ϕ are the amplitude to wavelength ratio and anisotropy factor respectively at azimuth ϕ, measured clockwise to the slip direction, and AF_{max} is a maximum anisotropy factor of γ_{90}/γ_0. Variations of K, γ_0 and AF_{max} at different wavelengths are summarized in Table 1. For example, γ_ϕ at $\lambda = 1$ m is less than at $\lambda = 15$ cm, but K is essentially the same at both wavelengths. However, K at $\lambda > 1$ m is significantly larger than K at $\lambda \leq 1$ m. The ratio AF_{max} increases markedly at $\lambda \approx 1$ m, varying from ≈ 1.9 at $\lambda \leq 1$ m to ≈ 4.5 at $\lambda \geq 1$ m. A similar change in γ_{90}/γ_0 can be observed in the power spectral plots produced by Power & Tullis (1991), although they did not discuss the implications. We suspect that this variation reflects a fundamental change in the dominant processes creating fault topography at scales below and above about 1 m. The azimuthal scaling function provides information for
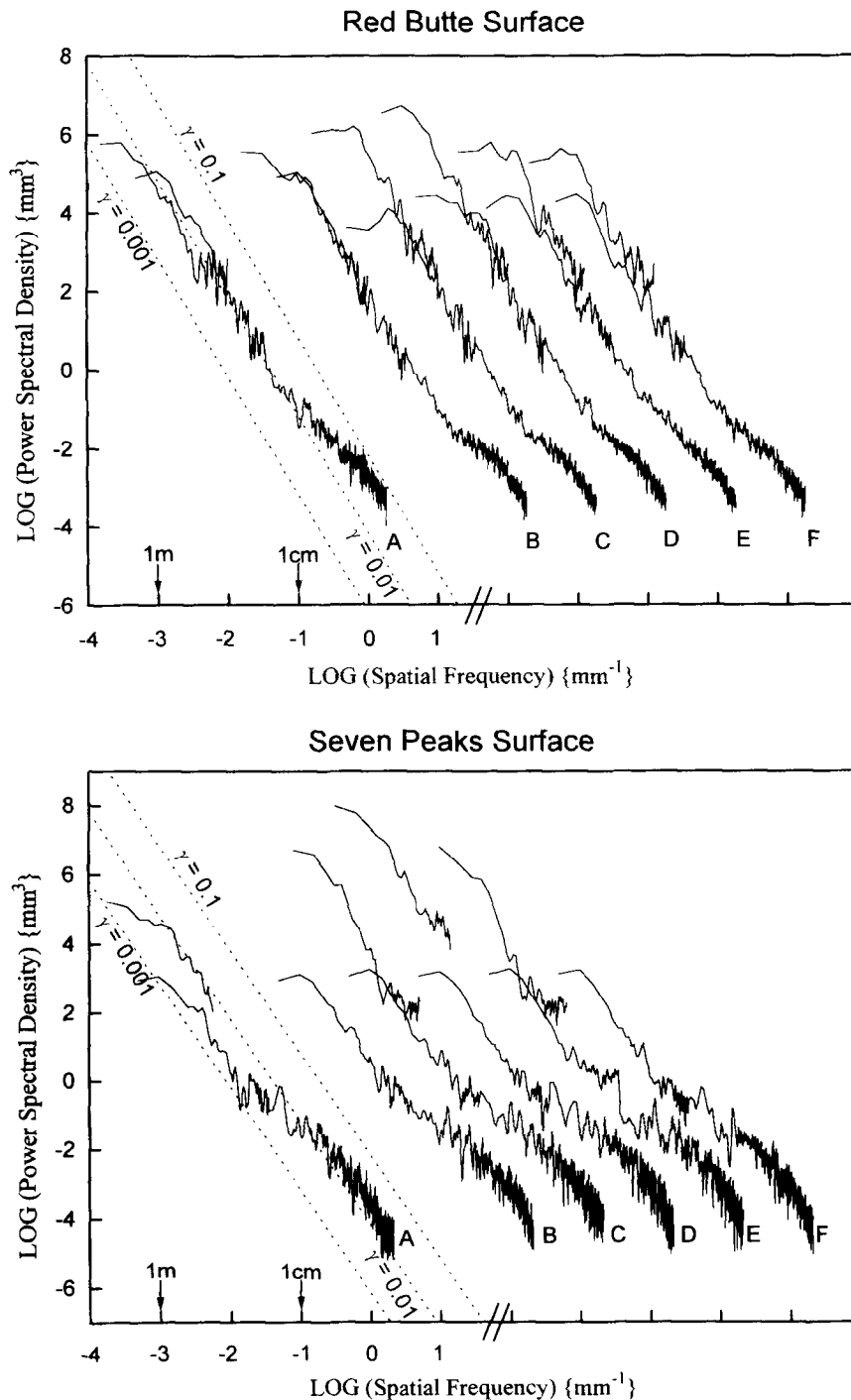
Fig. 6. Ensembled power spectra for two fault surface profiles. Dashed lines are contours of constant amplitude to wavelength ratio (γ) which allow easier visual interpretation of the spectra. The lower line and higher line represent $\gamma = 10^{-3}$ and $\gamma = 10^{-1}$, respectively. Note that each profile is characterized by a slope and intercept as shown in the idealized model of Fig. 3. In this figure, the profiles are plotted to scale, with each profile to the right of profile A referenced to the log(spatial frequency) = 0 bar on the horizontal axis below the profile. A: parallel to slip. B: 30° to slip. C: 60° to slip. D: perpendicular to slip. E: 120° to slip. F: 150° to slip. Note that the slopes and the intercepts are not constant for profiles within a given fault surface.

quantitative modeling of directional anisotropy, which is important for modeling fault geometry with the algorithm of Brown (1995).

Comparison with profiles of larger-scale fault surfaces

Extrapolation of fault surface properties from outcrop to larger scales is crucial to predicting the large-scale

geometry of fault surfaces at dimensions that are not usually available for direct measurement. Brown & Scholz (1985) note that such extrapolation is hindered by changes in fractal dimension between different length scales. The problem is further compounded by the effects of fault surface anisotropy. Power spectra from fault surfaces of different size are marked by significant changes in α and the intercept ($\log(C)$). Profiles measured
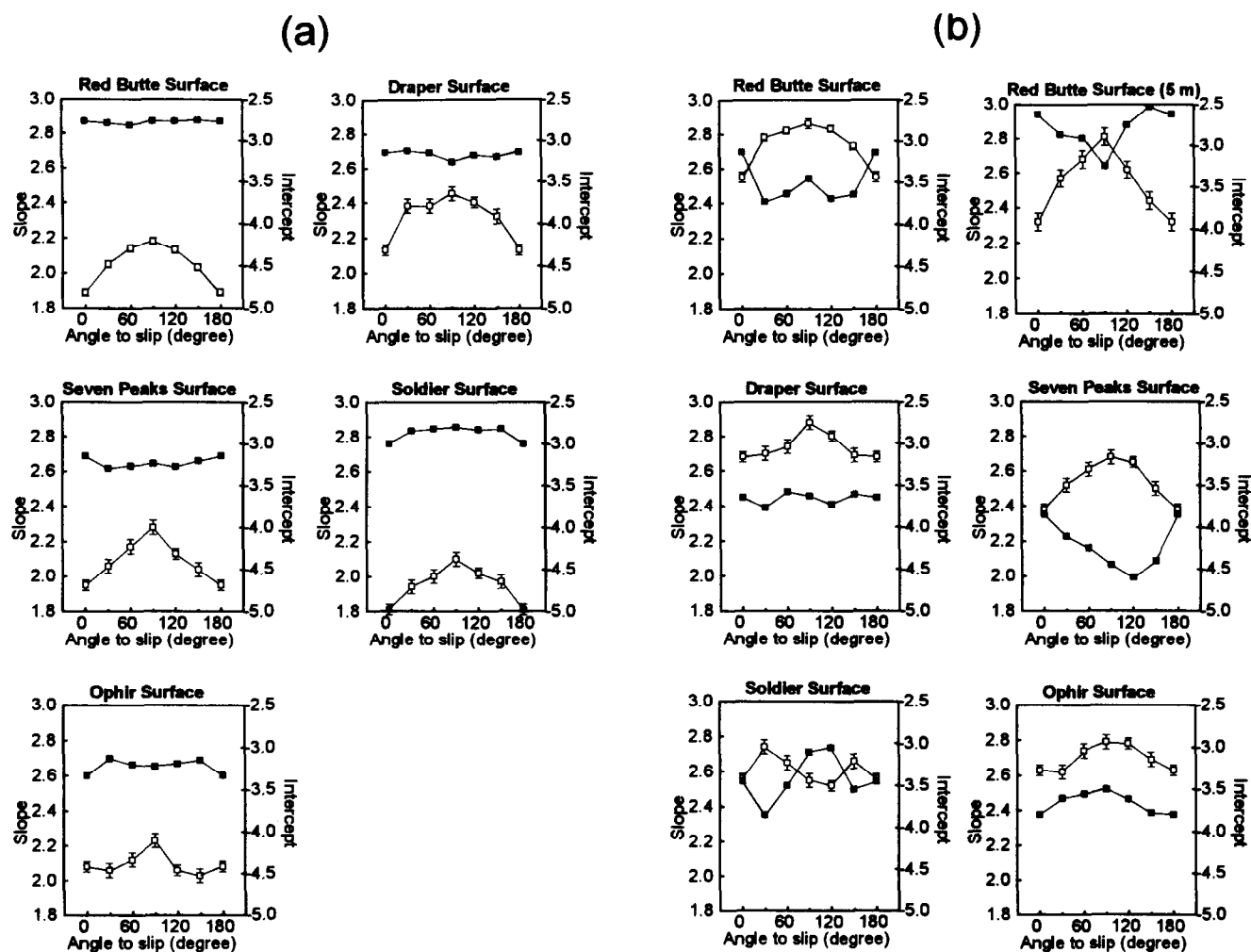
(a) **(b)**

Fig. 7. The relationship between angle to slip direction along fault surface and slope (α) and intercept ($\log(C)$) of the power spectra for surfaces at each study site. (a) Short profiles of 15 cm length, (b) longer profiles of 1.2 m length. Note that α (open squares) increases gradually from the direction parallel to slip to the direction perpendicular to slip for all surface profiles. The intercept, however, is more variable. Note that $\log(C)$ (solid squares) fluctuates much more for longer profiles (b) than shorter ones (a). These variations in α and $\log(C)$ are discussed in detail in the text. Refer to Fig. 3 for definition of slope (α) and $\log(C)$. Error bars indicate 1 standard deviation about the preferred value.

Table 1. Variation of K, γ_0, γ_{90}, and γ_{90}/γ_0 (Anisotropy Factor = $K/\gamma_0 + 1$) at different scales

Surface	15 cm scale				1 m scale				several (4–10) meter scale			
	K	γ_0	γ_{90}	γ_{90}/γ_0	K	γ_0	γ_{90}	γ_{90}/γ_0	K	γ_0	γ_{90}	γ_{90}/γ_0
Red Butte	4.10 (±0.40)	10.70 (±0.40)	14.80 (±0.40)	1.38	5.70 (±0.26)	6.80 (±0.26)	12.50 (±0.26)	1.84	10.40 (±0.65)	3.10 (±0.65)	13.50 (±0.65)	4.36
Draper	5.30 (±0.37)	7.90 (±0.37)	13.20 (±0.37)	1.67	4.60 (±0.43)	5.90 (±0.43)	10.50 (±0.43)	1.78				
Seven Peak	0.355 (±0.06)	3.10 (±0.06)	3.455 (±0.06)	1.12	0.76 (±0.05)	1.70 (±0.05)	2.46 (±0.05)	1.48	17.30 (±0.20)	3.70 (±0.20)	21.00 (±0.20)	5.68
Soldier	4.60 (±0.17)	6.90 (±0.17)	11.50 (±0.17)	1.67	3.40 (±0.31)	5.60 (±0.31)	9.00 (±0.31)	1.61	11.90 (±0.56)	3.60 (±0.56)	15.50 (±0.56)	4.31
Ophir	8.40 (±0.38)	5.65 (±0.38)	14.05 (±0.38)	2.49	6.20 (±0.75)	4.13 (±0.75)	10.33 (±0.75)	2.50	9.60 (±0.48)	3.90 (±0.48)	13.50 (±0.48)	3.46
Average	4.55 (±0.24)	6.85 (±0.24)	11.40 (±0.24)	1.66	4.13 (±0.36)	4.86 (±0.36)	8.96 (±0.36)	1.84	12.30 (±0.48)	3.58 (±0.48)	15.88 (±0.48)	4.43

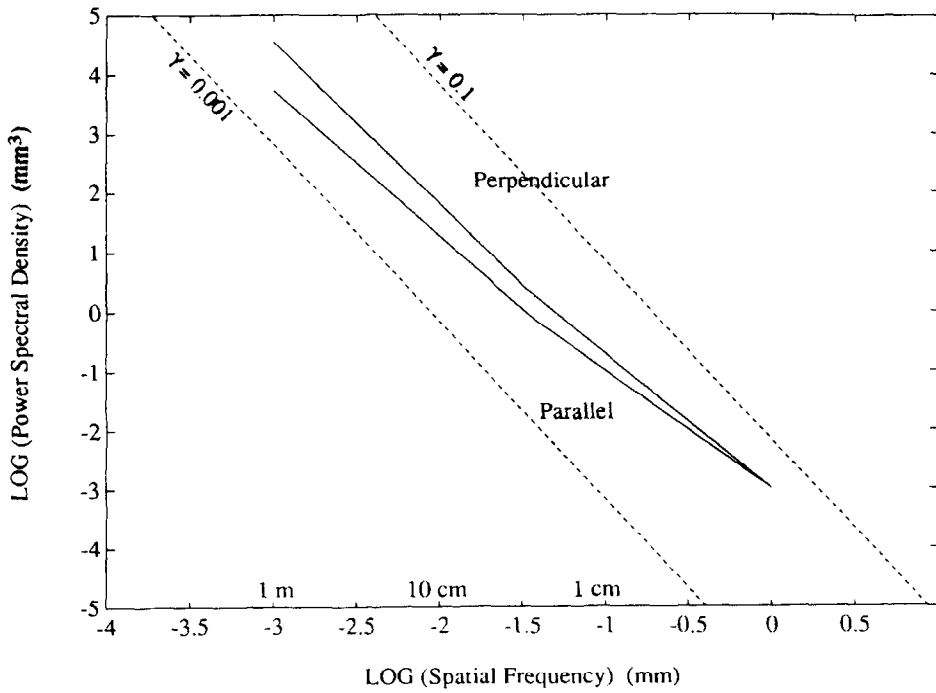All values are multiplied by 10^{-3} except anisotropy factor.

Fig. 8. Summary figure illustrating how the change in the slope and intercept of the power spectra occurs at spatial frequency between 10^{-1} and 10^{-2} mm^{-1} at wavelengths below 1 m. Note that the slope is greater and the intercept is less at wavelengths above 5–10 cm than at shorter wavelengths. Wavelength (λ) is written in cm above spatial frequency axis for reference.

perpendicular to fault slip direction are nearly self-similar ($\alpha \approx 3$) at wavelength $\lambda > 1$ m and $\gamma_\phi = 10^{-2}$ to 10^{-1} (Fig. 10). This is in contrast to profiles shorter than 1 m, which are characterized by self-affine scaling ($\alpha < 3$) and an amplitude to wavelength ratio (γ_ϕ) that increases as wavelength decreases (i.e. ranging from $\approx 10^{-1}$ to 10^{-3} at 1 mm $< \lambda < 1$ m).

Amplitude data from surface outcrops and digitized mine maps are plotted against models of γ versus λ for directions parallel (Fig. 11a) and perpendicular to slip (Fig. 11b) using equation (7). The fractal dimension for slip parallel profiles is $D \approx 1.2$ for $\lambda < 5$ m, and $D \approx 1.1$ for 60 m $< \lambda < 150$ m (Fig. 11a). D is similar for profiles oriented perpendicular to slip direction, but there is a
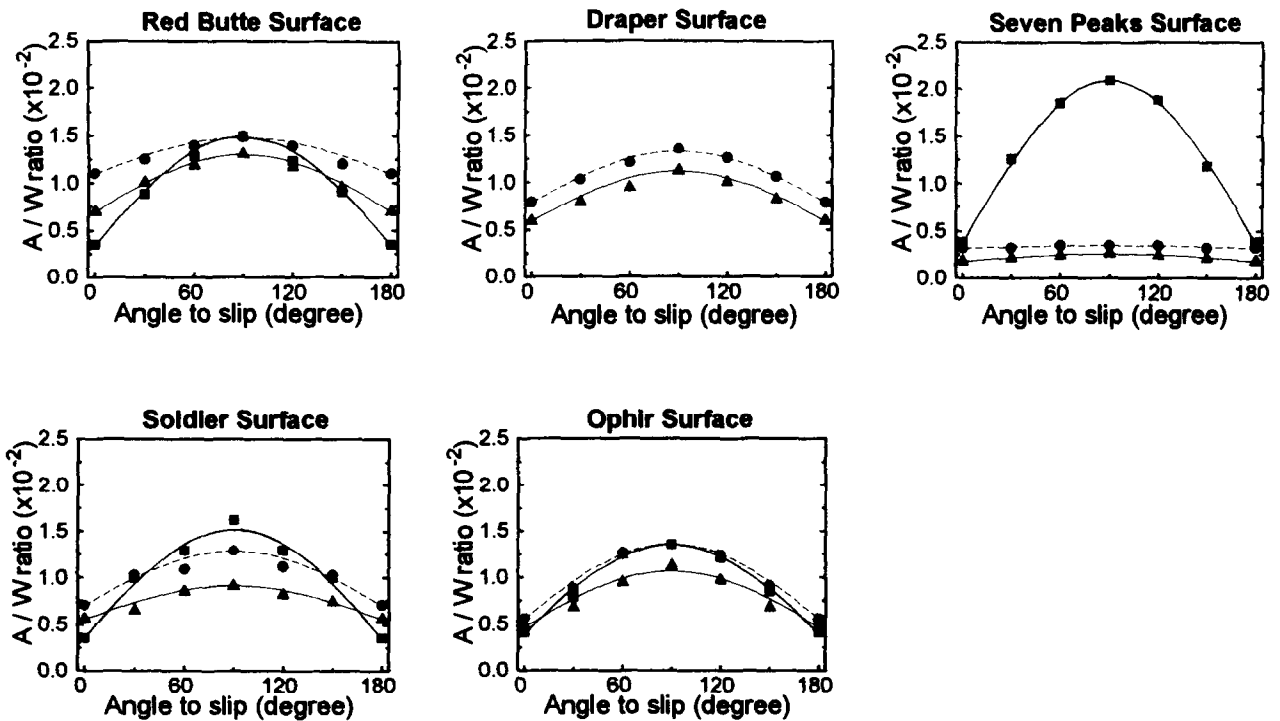

Fig. 9. The relationship between the angle to slip direction and the amplitude to wavelength ratio (γ) for each natural fault surface studied. Solid circles denote data at $\lambda \leq 15$ cm, solid triangles for 15 cm $< \lambda \leq 1$ m, and solid squares for $\lambda > 1$ m. Note that the variation of amplitude to wavelength ratio (γ) is well fitted with a simple sine curve.

(a) Wasatch fault zone
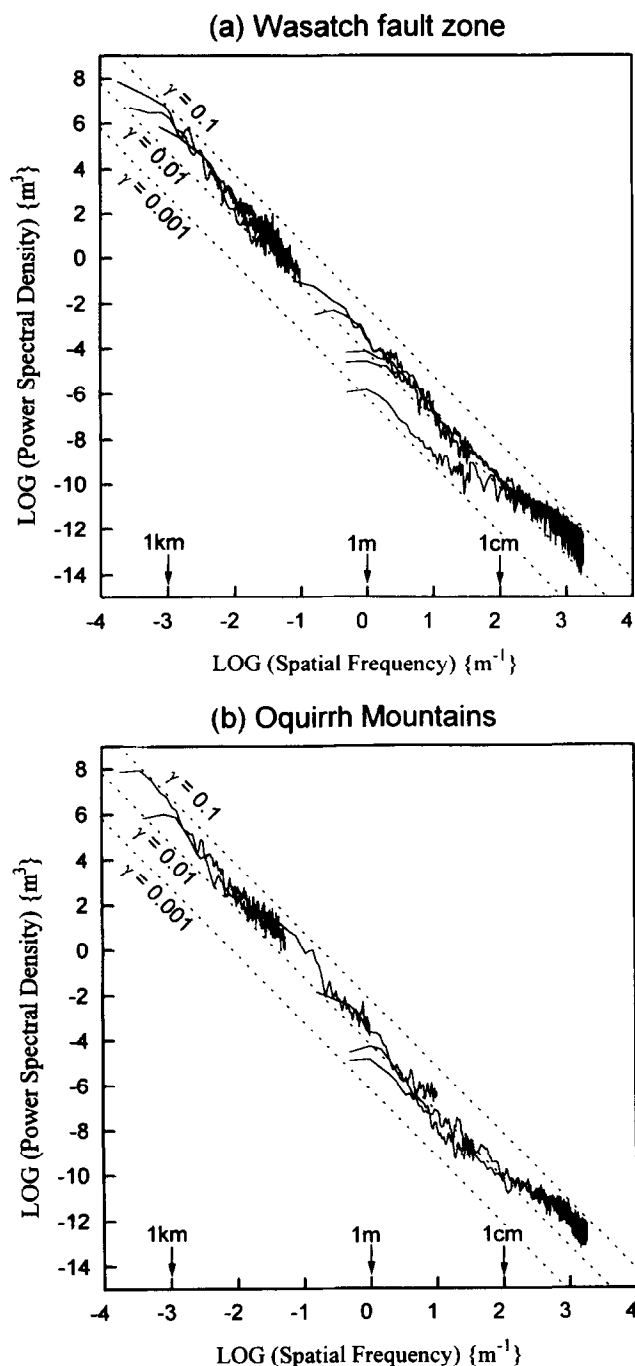

(b) Oquirrh Mountains

Fig. 10. Power spectra for profiles approximately perpendicular to the slip direction for a large wavelength bandwidth between 10 mm to about 5 km from natural fault surfaces along (a) the Wasatch fault zone and (b) the Oquirrh Mountains. Fault surface spectra were calculated from outcrop profiles and digitized profiles taken from maps. Dashed lines are contours of constant amplitude to wavelength ratio (γ) which allow easier visual interpretation of the spectra. The lower lines and the higher lines represent $\gamma = 10^{-3}$ and $\gamma = 10^{-1}$, respectively.

significant change in the intercept ($\log(C)$) of the power spectra (Fig. 11b). $D \approx 1.15$ for $\lambda < 1$ m, and decreases to $D \approx 1.05$ for 1 m $< \lambda < 150$ m. The intercept ($\log(C)$) of the power spectra for $\lambda < 5$ m is less than the intercept for $\lambda > 5$ m, which causes a significant change in γ_{90} between the two different wavelength bands (Fig. 11b). Another important change in scaling may take place at $\lambda \approx 3$ km above which $D \approx 1.0$. For $\lambda > 3$ km, there is a change in

intercept ($\log(C)$) in the power spectra, and an accompanying change in the trend of γ_ϕ as a function of λ. However, the traces of fault zones at scales greater than several tens of meters probably represent the linking together of several fault surfaces, and perhaps should not be directly compared with the single surface profile measurements made at smaller scale.

DISCUSSION

Scaling property change and processes for the evolution of surface roughness

Chen & Spetzler (1993) noted slope breaks in power spectra within several different wavelength bands from both artificial sliding surfaces and natural fault surfaces and fault zones. This observation is based upon their own laboratory experiments and the re-examination of previous results (Scholz & Aviles 1986, Aviles et al. 1987, Okubo & Aki 1987, Power et al. 1987). For their experimental work, Chen & Spetzler (1993) suggest that the break in slope at wavelengths of several millimeters is caused by a change in the dominant mode of deformation from small-scale intergranular cracking to intragranular cracking at a larger scale.

We also observe changes of power spectra slope and shift of intercept between different wavelength bands in this study (Figs. 6, 8 and 10). The scaling parameters of the natural fault surfaces change as a function of wavelength, and can be approximated as constants only within discrete wavelength bands (Table 2). This is particularly clear for profiles measured perpendicular to slip direction, but can also be detected from profiles measured parallel to slip, along which additional wear during sliding may reduce the sharpness of fault intersections and offsets. Presumably, this variation in scaling parameters reflects different processes operating at different spatial scales. For example, a significant increase in slope with a decrease in intercept of power spectra exists in the wavelength band of several cm $< \lambda < 15$ cm (Fig. 8), which reflects a change in characteristic roughness of fault surfaces at this wavelength. Another change in slope and intercept of power spectra, as reflected in K and AF, occurs at $\lambda \approx 1$ m (Table 2). Notably, single slip events on large faults during M = 6–7 earthquakes are typically of the order of several meters or less, and perhaps roughness in this wavelength band (1 mm $< \lambda <$ several m) reflects a combination of frictional ploughing, secondary fracturing, and intersections between anastomosing fractures along sliding surfaces. Pitting of surfaces by weathering may also contribute to roughness within this wavelength band (Power & Tullis 1991). At $\lambda >$ several meters, roughness may reflect the processes of lateral growth and linking together of several fault surfaces, both during the early evolution of the fault zone or during subsequent faulting as new secondary faults are generated and older ones become inactive.
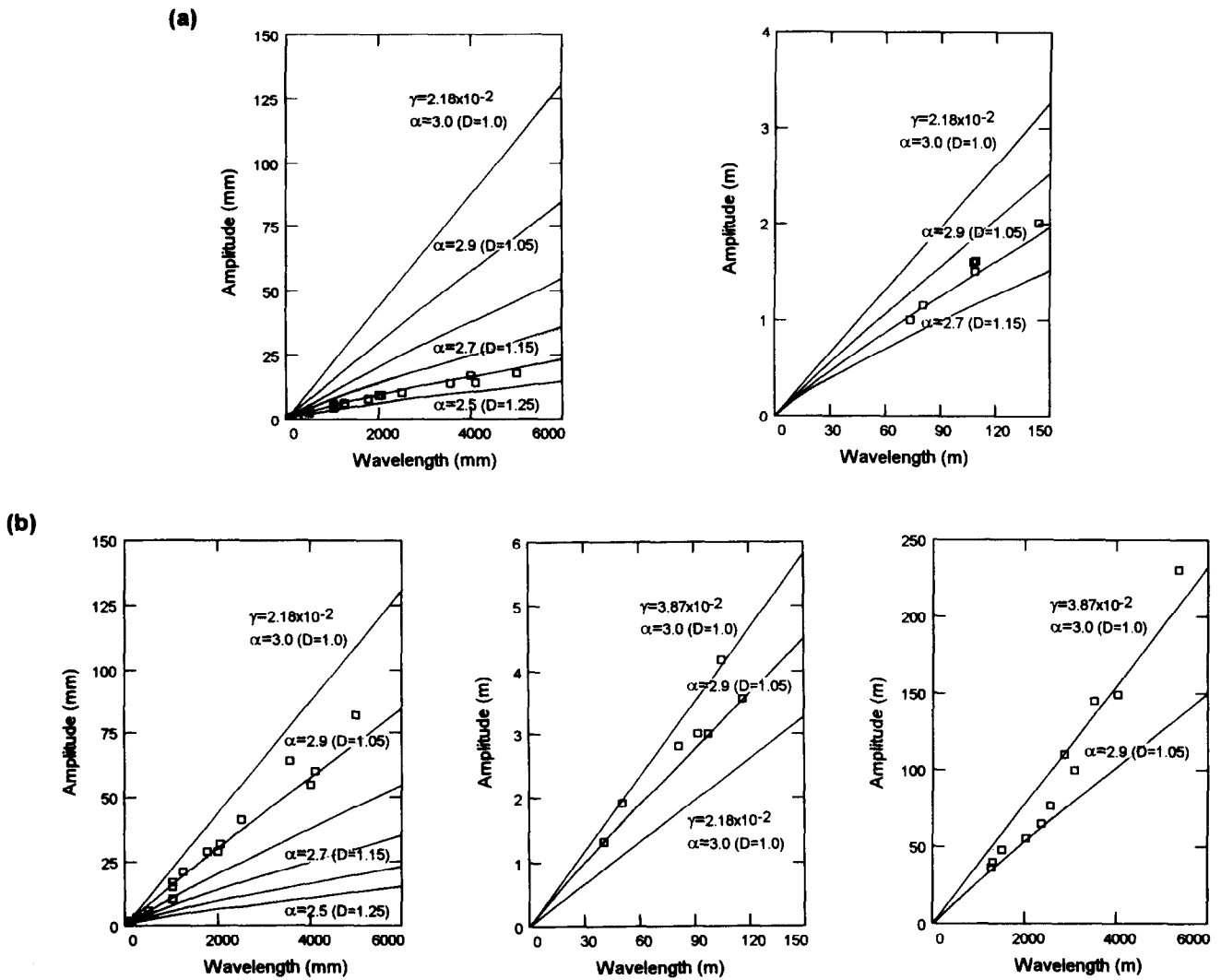
Fig. 11. Amplitude to wavelength ratio as function of wavelength (λ) for several bandwidths between 1 m and several km. (a) Increase of amplitude to wavelength ratio parallel to slip direction at fixed average intercept, $\log(C)_{avg} = -3.50$. (b) Increase of amplitude to wavelength ratio perpendicular to slip direction at fixed average intercepts, $\log(C)_{avg} = -3.50$ and $\log(C)_{avg} = -3.0$.

Fractal models of natural fault surfaces

The fractal dimension (D), intercept ($\log(C)$) of power spectra, anisotropy factor (AF), and profile variance (Table 2) provide the parameters needed to generate fractal models of natural fault surfaces. The algorithm of Brown (1995) is an appropriate starting point for modeling anisotropic surfaces of specified fractal dimension and anisotropy. This algorithm is based on the spectral synthesis method as discussed by Saupe (1988).

A model surface is generated by taking the two-dimensional, inverse Fourier transform of a synthesized amplitude spectrum, which is computed by specifying the fractal dimension (D) and anisotropy factor (AF_{max}). The resulting corrugated surfaces appear similar to natural fault surfaces, but the algorithm does not explicitly take into account the azimuthal variation in anisotropy factor (AF_ϕ), fractal dimension (D), nor intercept ($\log(C)$) that we observe in our measurements. We have modified Brown's algorithm to account

Table 2. The variation in scaling parameters including γ_0, γ_{90} and K for different wavelength bands

Parameter	15 cm-scale	1 m-scale	several m-scale	hundred m-scale	several km-scale
γ_0 ($\times 10^{-3}$)	6.85 (± 0.24)	4.86 (± 0.36)	3.58 (± 0.48)	14.1 (± 2.00)	14.0 (?)
γ_{90} ($\times 10^{-3}$)	11.40 (± 0.24)	8.96 (± 0.36)	15.58 (± 0.48)	33.0 (± 2.50)	34.9 (± 4.10)
K	4.55 (± 0.24)	4.13 (± 0.36)	12.30 (± 0.48)	18.9 (± 2.13)	20.9 (?)
AF_{max}	1.7	1.9	4.5	2.4	2.5 (?)
D	1.53 (± 0.03)	1.26 (± 0.03)	1.25 (± 0.04)	≈ 1.10	≈ 1.05
$\log(C)_{avg}$	-3.06 (± 0.03)	-3.50 (± 0.20)	-3.48 (± 0.20)	≈ -3.5	

explicitly for the observed azimuthal variation in AF_ϕ, to incorporate explicitly the intercept of the power spectrum for scaling purposes, and to allow the fractal dimension (D) to be specified as a function of azimuth (Appendix). We do not take account of azimuthal variation in log(C), but use an average value. Figure 12 graphically illustrates the difference in power spectra of models with directional variation in one or more of these parameters. First we compare the difference between Brown's algorithm and the one in which $AF(\phi)$ is explicitly computed as a function of azimuth by showing the difference between two fractal fault surfaces, one generated with fixed AF_{max} (Brown's algorithm) and the other with azimuthal variation in AF_{max} given by equation (11). There is little difference between the two surfaces, which indicates that specification of the maximum anisotropy ratio is adequate for modeling purposes, if fractal dimension (D) is constant. We also compare the difference between two fractal fault surfaces, one generated with fixed AF_{max} and the other with azimuthal variation in D, using represen-

tative parameters indicated by our measurements. The intercept (log(C)) is the same in both models. D varies smoothly from 2.26 parallel to slip direction to 2.06 perpendicular to slip direction. There is a large difference between the textures of the two surfaces, demonstrating that azimuthal variation in D may be an important feature to incorporate in modeling algorithms.

Fault surfaces modeled by varying D as a function of azimuth (ϕ) contain elongate corrugations parallel to slip direction, but are more strongly 'cross corrugated' than those generated with constant D (Fig. 13). This difference in surface texture is an important control on the geometrical properties of aperture generated by sliding of opposing fault walls (Fig. 14). The aperture distribution is less anisotropic for the faults with azimuthal variation in D than for those with fixed D. There is better connectivity between void space in the former models than in the latter type, because of the cross corrugated surface texture. This difference may be particularly significant for creating better frictional models of faulting (Power & Tullis 1992), understanding fault hydrology (Thompson & Brown 1991) and predicting the geometry of fault controlled ore deposits (Brown & Bruhn 1996).

The processes or features responsible for creating fault surfaces with azimuthal variation in fractal dimension (D) require further study, but two mechanisms seem particularly significant after considering structural relationships in outcrops and published observations by mine geologists (Newhouse 1940). These field observations are relevant to the subsidiary cross corrugation texture developed in the fractal fault surface models based on azimuthal variation in D (Fig. 13). Refraction of fault surfaces across lithologic boundaries such as bedding, unconformities and igneous or metamorphic rock contacts gives rise to cross-corrugations trending at various angles to slip direction, depending upon the orientation of the contacts (Guilbert & Park 1986, Roscoe 1951). The main fault surface may also be cut by secondary faults, such as R and R' shears (Fig. 15, Petit 1988, Tchalenko 1970). If these faults are activated during rupturing on the main surface, they will locally offset and warp the main fault surface into complex corrugations that appear at least qualitatively similar to those generated by the fractal model with azimuthal variation in fractal dimension (D) (Fig. 13). This type of structural relationship between primary and secondary faulting is observed on the large surface of the Wasatch fault at the Seven Peaks locality.

Fault models like those in Fig. 13 provide a starting point for investigating a number of problems: predicting subsurface fault structure from sinuous scarps (Bruhn et al. 1991), understanding fluid transport and ore deposition in fault controlled mineral deposits (Thompson & Brown 1991, Brown & Bruhn 1996), and modeling the secondary fracturing and brecciation in rocks surrounding fault surfaces (Petit 1988), among others. Establishing correlations between dimensional properties of fault corrugations, frequencies of earthquake source coda, and perhaps aftershock distributions is another potential area of research (Ben-Zion & Rice 1995).
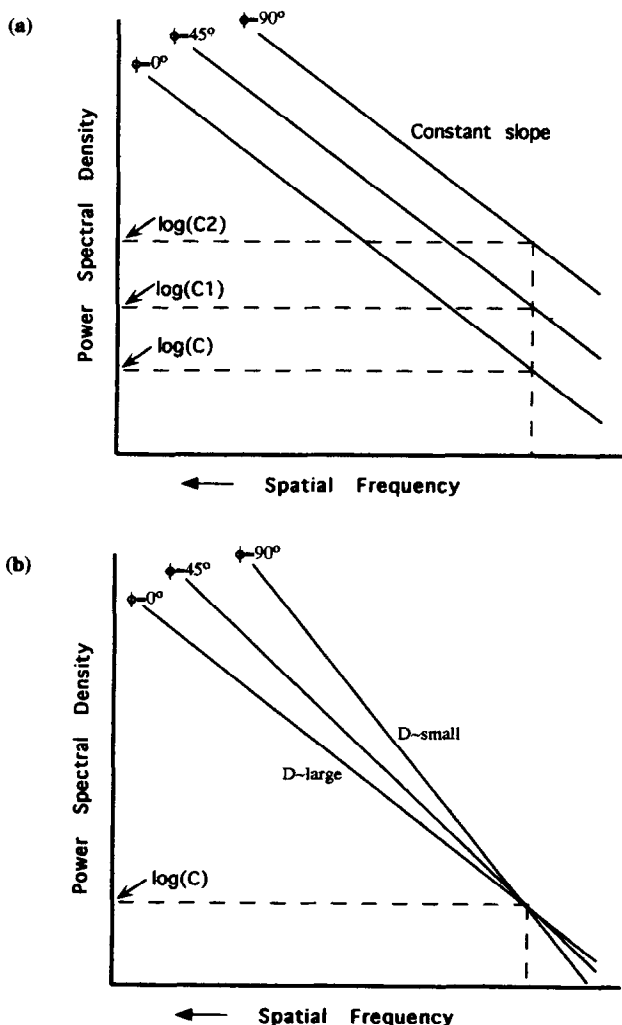

Fig. 12. Graphical illustration of the difference in power spectral models generated by azimuthal variation in scaling parameters. (a) Azimuthal variation in intercepts (log(C)). (b) Azimuthal variation in fractal dimension (D).
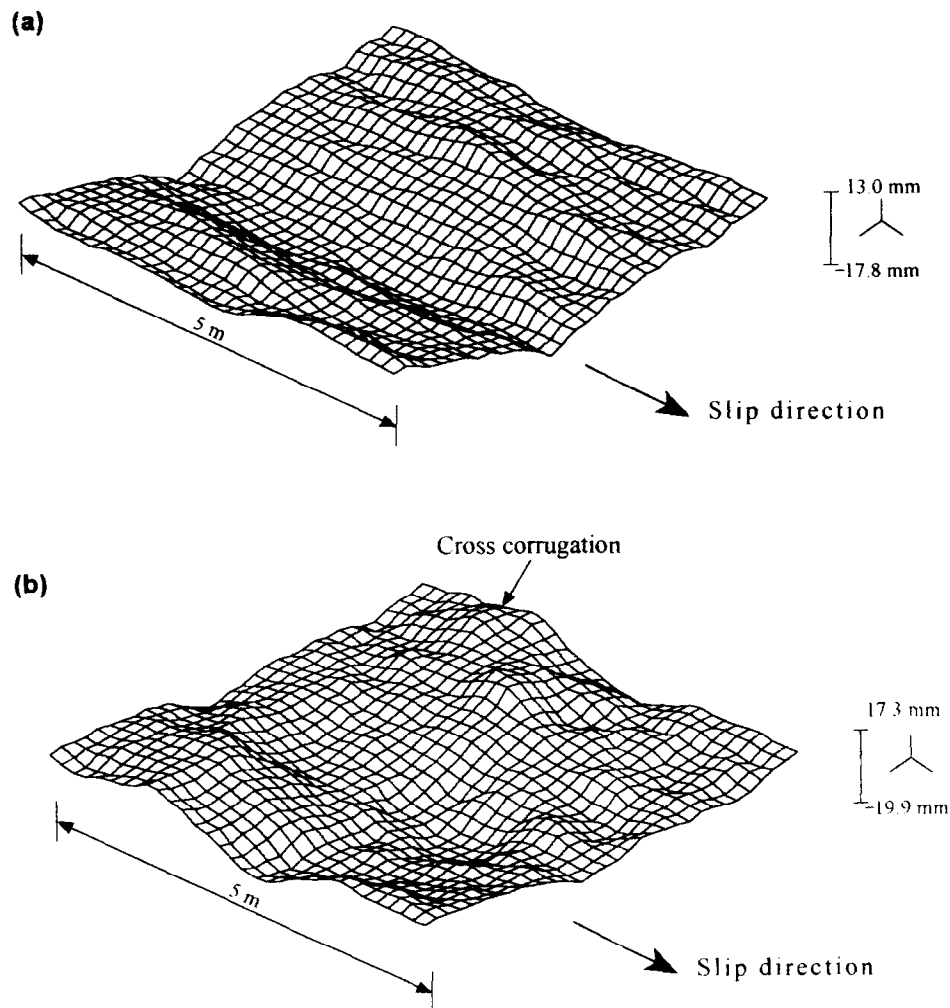
Fig. 13. Example of fractal models of natural fault surfaces using the modified algorithm in the Appendix with fixed average intercept, $\log(C)_{avg} = -3.5$. (a) Azimuthal variation in AF with constant D. AF_ϕ varies from 1.0 parallel to slip direction to 4.5 perpendicular to slip and D is 2.26. (b) Azimuthal variation in D. $D(\phi)$ varies from 2.26 parallel to slip direction to 2.06 perpendicular to slip and AF_{max} is 4.5. Note the stronger cross corrugations than in (a).

CONCLUSION

Fractal geometry (Mandelbrot 1983) can be used to characterize a natural fault surface. However, a single fractal dimension does not adequately describe the spatial scaling because the scaling parameters such as the slope (fractal dimension) and intercept of power spectra strongly depend on the azimuth in the fault surface and the wavelength band considered. The spatial scaling of fault surfaces is self-affine within the wide wavelength range of 1 mm to approximately 5 km.

The directional anisotropy of a natural fault surface is described by an azimuthal scaling function, $\gamma_\phi = K \sin(\phi)$ + γ_0 or $AF_\phi = (AF_{max} - 1) \sin(\phi) + 1$, where γ_ϕ and AF_ϕ are the amplitude to wavelength ratio and anisotropy factor respectively at azimuth ϕ. K is an anisotropy coefficient and increases systematically with an increase of spatial wavelength on natural fault surfaces (Table 2). AF_{max} is the maximum anisotropy factor and ranges between 2.0 and 2.5 at all scales other than λ > several meters, at which $AF_{max} = 4.5$ for the surfaces measured in this study.

Different processes probably dominate in generating surface textures at different spatial scales. Frictional wearing by secondary fracturing during rupturing, and ploughing of asperities are likely processes that dominate surface texture at scales of a few meters and less. Pitting of the surfaces by weathering is a potential problem in interpreting power spectra at short wavelengths, particularly in carbonate rocks, and care must be taken in selecting appropriate surfaces for measurement. At larger scales, geometrical irregularity created by linking together of fault surfaces, and intersections of lithologic contacts and mesoscopic secondary faults and joints with the primary fault surface become potentially important features in the surface texture.

The fractal dimension (D), intercept $(\log(C))$ of power spectra, and variation in anisotropy factor (AF), are needed to generate realistic fractal models of natural fault surfaces using spectral synthesis. The fault surface model generated with fixed D and azimuthal variation in AF_{max} shows a good approximation of natural fault surfaces. However, the fault surface model generated with azimuthal variation in D presents a better description of
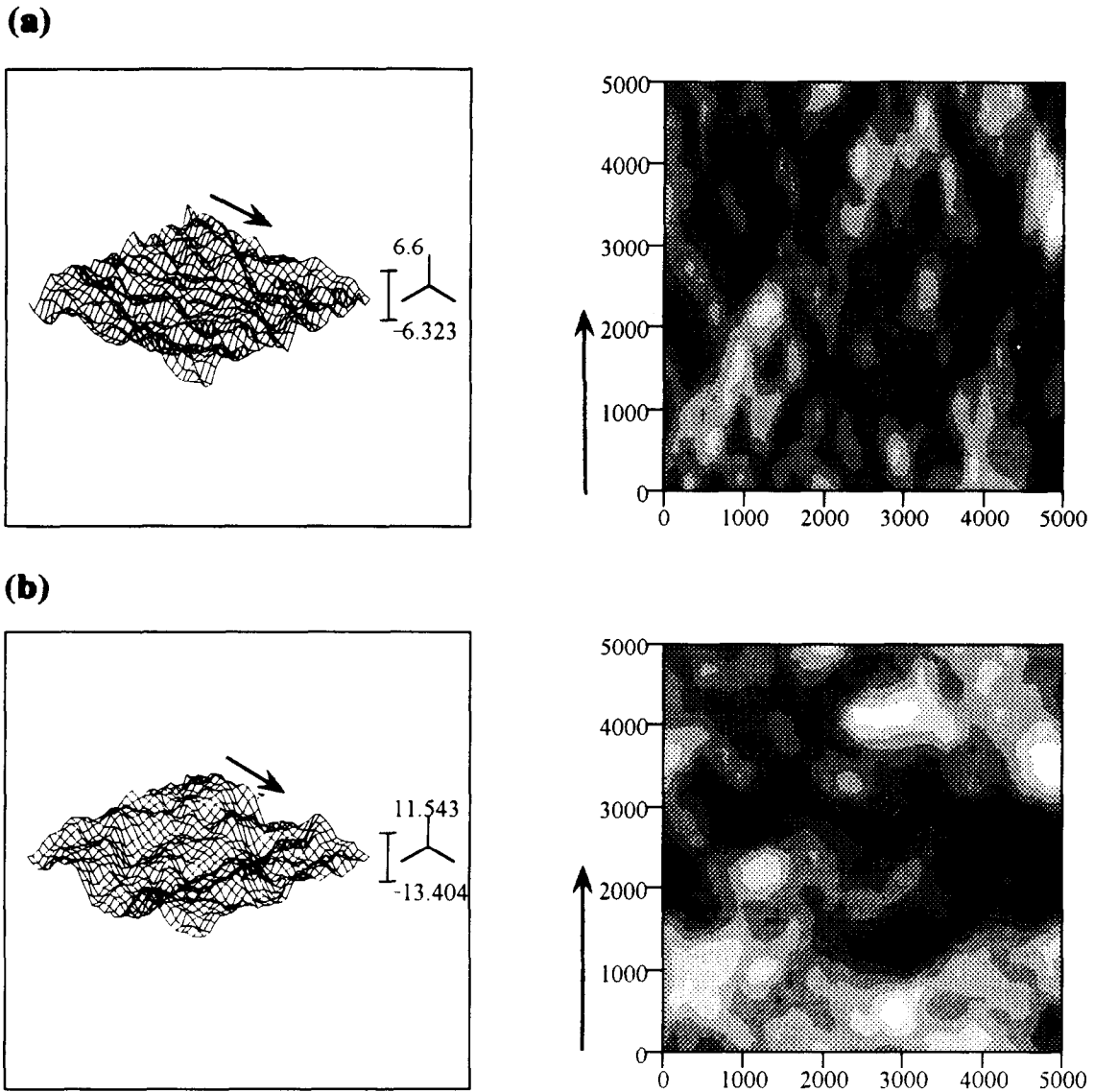
(a)

(b)

Fig. 14. Aperture distribution generated by sliding of opposing fault walls shown in Fig. 13 with offset of 483 mm in 5000 mm × 5000 mm fault surface. Arrows are parallel to the slip directions. (a) Oblique view (left) and contour map of aperture (right) between two surfaces generated with azimuthal variation in AF with constant D. (b) Oblique view (left) and contour map of aperture (right) between two surfaces generated with azimuthal variation in D. Low to high contour of apertures range from black to white. Note the more isotropic aperture distribution in (b) than in (a).
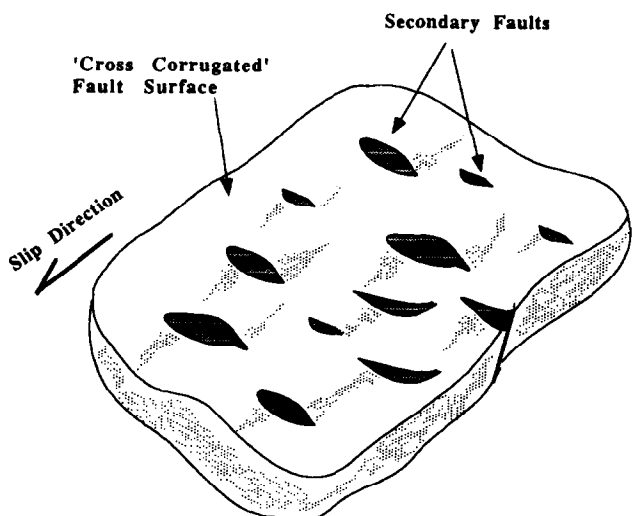

Fig. 15. Schematic diagram illustrates that cross corrugations approximately normal to slip direction may be formed by subsidiary faults. R shears are shown schematically in this example.

natural fault surfaces, showing cross corrugations with respect to slip direction. The latter fault model can be applied to predict the geometries of subsurface fault structures which create complex surface scarps, to model fluid transport and ore deposition in fault controlled mineral deposits, to generate models of secondary stresses in the adjacent wall rock, and to investigate the characteristics of the gouge zone generated during frictional sliding. Applications to earthquake source processes and aftershock distributions may also be explored in the future.

REFERENCES

Anderson, E. M. 1951. *The Dynamics of Faulting*, 2nd edn. Oliver & Boyd, Edinburgh.

Aviles, C. A., Scholz, C. A. & Boatwright, J. 1987. Fractal analysis applied to characteristic segments of the San Andreas fault. *J. geophys. Res.* **92**, 331–334.

Barton, N. R. 1986. Deformation phenomena in jointed rock. *Géotechnique* **36**, 147–167.

Berry, M. V. & Lewis, Z. V. 1980. On the Weierstrass–Mandelbrot fractal function. *Proc. R. Soc.* A **370**, 459–484.

Bendat, J. S. & Piersol, A. G. 1986. *Random Data: Analysis and Measurement Procedures*. John Wiley & Sons, New York.

Ben-Zion, Y. & Rice, J. R. 1995. Slip patterns and earthquake populations along different classes of faults in elastic solids. *J. geophys. Res.* **100**, 12,959–12,983.

Brown, S. R. 1987. Fluid flow through rock joints: The effect of surface roughness. *J. geophys. Res.* **92**, 1337–1347.

Brown, S. R. 1995. Simple mathematical model of rough fracture. *J. geophys. Res.* **100**, 5941–5952.

Brown, S. R. & Bruhn, R. L. 1996. Formation of voids and veins during faulting. *J. Struct. Geol.* **18**, 657–671.

Brown, S. R., Kranz, R. L. & Bonner, B. P. 1986. Correlation between the surfaces of natural rock joints. *J. geophys. Res.* **13**, 1430–1433.

Brown, S. R. & Scholz, C. H. 1985. Broad bandwidth study of the topography of natural rock surfaces. *J. geophys. Res.* **90**, 12,575–12,582.

Brown, S. R. & Scholz, C. H. 1986. Closure of rock joints. *J. geophys. Res.* **91**, 4939–4948.

Bruhn, R. L., Gibler, P. R. & Parry, W. T. 1987. Rupture characteristics of normal faults: An example from the Wasatch fault zone, Utah. In: *Continental Extensional Tectonics* (edited by Coward, M. P., Dewey, J. F. & Hancock, P. L.). *Geological Society of London Special Publication* **28**, 337–353.

Bruhn, R. L., Yang, Zhu-en, Wu, D. & Yonkee, A. W. 1991. Structure of the Warm Spring and northern Thousand Spring fault segments, Lost River fault zone, Idaho: possible effects on rupturing during the 1983 Borah Peak Earthquake. *Tectonophysics* **200**, 33–49.

Chen, G. & Spetzler, H. A. 1993. Topographic characteristics of laboratory-induced shear fractures. *Pure Appl. Geophys.* **140**, 123–135.

Crittenden, M. D., Jr. 1965. Geologic map of the Draper Quadrangle, Utah. *U.S. Geol. Surv. Map* GQ-378.

Gibler, P. R. 1985. Bedrock deformation along the Salt Lake segment of Wasatch fault: Implications for principal stress directions, principal stress magnitude, and seismicity. Unpublished MSc thesis, University of Utah.

Gilbert, G. U. K. 1928. Studies of basin-range structure. *U.S. Geol. Surv. Prof. Pap.* **153**.

Guilbert, C. F. & Park, J. M. 1986. *The Geology of Ore Deposits*. Freeman, New York.

Hintze, L. F. 1978. Geologic map of the Y mountain area, east of Provo, Utah. *Brigham Young University Geology Studies—Special Publication* 5.

Horn, R. V. & Crittenden, M. D., Jr. 1987. Map showing surficial units and bedrock geology of the Fort Douglas Quadrangle and parts of the Mountain Dell and Salt Lake City north Quadrangles, Davis, Salt Lake, and Morgan Counties, Utah. *U.S. Geol. Surv. Map* I-1742.

Kamb, B. 1970. Sliding motion of glaciers: Theory and observation. *Rev. Geophys.* **8**, 673–728.

Machette, M. N., Personius, S. F. & Nelson, S. R. 1987. Quaternary geology along the Wasatch fault zone: segmentation, recent investigations, and preliminary conclusions. *U.S. Geol. Surv. Open-File Report* **87-585** I, A1–A72.

Machette, M. N., Personius, S. F. & Nelson, S. R. 1991. The Wasatch fault zone—segmentation and history of Holocene earthquakes. *J. Struct. Geol.* **13**, 137–151.

Mandelbrot, B. B. 1967. How long is the coastline of Britain? Statistical self-similarity and fractional dimension. *Science* **156**, 636–638.

Mandelbrot, B. B. 1983. *The Fractal Geometry of Nature*. W. H. Freeman, New York.

Newhouse, W. H. 1940. Openings due to movement along a curved or irregular fault plane. *Econ. Geol.* **35**, 445–464.

Nolte, D. D., Pyrak-Nolte, L. J. & Cook, N. G. W. 1989. The fractal geometry of flow paths in natural fractures in rock and the approach to percolation. *Pure & Appl. Geophys.* **131**, 111–138.

Nye, J. F. 1970. Glacier sliding without cavitation in a linear viscous approximation. *Proc. R. Soc.* A**315**, 381–403.

Okubo, P. G. & Aki, K. 1987. Fractal geometry in the San Andreas fault system. *J. geophys. Res.* **92**, 345–355.

Petit, J.-P. 1988. Normal stress dependent rupture morphology in direct shear tests on sandstone with applications to some natural fault surfaces. *Int. J. Rock Mech. Min. Sci. and Geomech. Abstr.* **25**, 411–419.

Power, W. L. & Tullis, T. E. 1991. Euclidean and fractal models for the description of rock surface roughness. *J. geophys. Res.* **96**, 415–424.

Power, W. L. & Tullis, T. E. 1992. The contact between opposing fault surfaces at Dixie Valley, Nevada, and implications for fault mechanics. *J. geophys. Res.* **97**, 15,425–15,435.

Power, W. L., Tullis, T. E., Brown, S. R., Boitnott, G. N. & Scholz, C. H. 1987. Roughness of natural fault surfaces. *Geophys. Rev.* **14**, 29–32.

Power, W. L., Tullis, T. E. & Weeks, J. D. 1988. Roughness and wear during brittle faulting. *J. geophys. Res.* **93**, 15,268–15,278.

Roscoe, S. M. 1951. Dilation maps, their application to vein-type ore deposits. Unpublished PhD Thesis, Stanford University.

Saupe, D. 1988. Algorithms for random fractals. In: *The Science of Fractal Images* (edited by Peitgen, H. O. & Saupe, D.). Springer-Verlag, New York, 71–136.

Scholz, C. H. 1987. Wear and gouge formation in brittle faulting. *Geology* **15**, 493–495.

Scholz, C. H. 1990. *The Mechanics of Earthquakes and Faulting*. Cambridge University Press, Cambridge.

Scholz, C. H. & Aviles, C. A. 1986. The fractal geometry of faults and faulting. In: *Earthquake Source Mechanics* (edited by Das, S., Boatwright, J. & Scholz, C. H.). *Geophys. Monogr. Ser.* **37**, 147–155.

Schwartz, D. P. & Coppersmith, K. J. 1984. Fault behavior and characteristic earthquakes: Examples from the Wasatch and San Andreas fault zones. *J. geophys. Res.* **89**, 5681–5698.

Tchalenko, J. S. 1970. Similarity between shear zones of different magnitudes. *Bull. geol. Soc. Am.* **81**, 1625–1640.

Thompson, M. E. & Brown, S. R. 1991. The effect of anisotropic surface roughness on flow and transport in fracture. *J. geophys. Res.* **96**, 21,923–21,932.

Voss, R. F. 1988. Fractals in nature: From characterization to simulation. In: *The Science of Fractal Images* (edited by Peitgen, H. O. & Saupe, D.). Springer-Verlag, New York, 21–70.

Wang, J. S. Y., Narashimhan, T. N. & Scholz, C. H. 1988. Aperture correlation of a fractal fracture. *J. geophys. Res.* **93**, 2216–2224.

Wu, D. & Bruhn, R. L. 1994. Geometry and kinematics of active normal fault along the western flank of the southern Oquirrh mountains, Utah: implication for fault growth. *J. Struct. Geol.* **16**, 1061–1075.

APPENDIX

ALGORITHM		Fault surface (X, N, Hur, Seed, Phi)
Title		Fractal fault surface with variable fractal dimension
Arguments	X[ ][ ]	array of complex values of size NxN
	N	size of array X along one dimension
	Hr, Hl	Hurst exponent perpendicular and paralle to slip direction
Variables	j,k,j0,k0	integers
	Rad, Phase	polar coordinates for Fourier coefficient
	Phi	angle to slip direction
	Hur	Hurst exponent at angle to slip direction
	A[ ][ ]	array of complex variables of size NxN
Functions	Angle( )	gets angle from array index
	RandNum( )	returns a random number
	InvFFT2D	fast Fourier transform in two dimensions

```
BEGIN
    InitRandNum(Seed);
    FOR j: = 0 TO N/2 DO
        FOR k: = 0 TO N/2 DO
            Phase: = 2 * 3.14159 * RandNum ();
            IF (j > 0 AND k > 0) THEN Phi: = Angle();
            ELSE
                IF (k: = 0) THEN Phi: = 0;
                ELSE Phi: = 3.14159/2;
                END IF
            END IF
            Hur: = (Hr-Hl) * sin(Phi) + Hl;
            IF (j ≠ 0 AND k ≠ 0) THEN Rad: = power(j*j + k*k,-(Hur + 1)/2);
            ELSE Rad: = 0;
            END IF
            A [j][k]: = (Rad * cos(Phase) + Rad * sin(Phase));
            IF (j = 0) THEN j0: = 0;
            ELSE j0: = N-j;
            END IF
            IF (k = 0) THEN k0: = 0;
            ELSE k0: = N-k;
            END IF
            A [j0][k0]: = (Rad*cos(Phase)-Rad*sin(Phase));
        END FOR
    END FOR
    A[N/2][0].img: = 0;
    A[0][N/2].img: = 0;
    A[N/2][N/2].img: = 0
    FOR j: = 1 TO N/2 - 1 DO
        FOR k: = 1 TO N/2 - 1 DO
            Phase: = 2 * 3.14159 * RandNum( );
            Rad: = power (j*j + k*k,-(Hur + 1)/2);
            A[j][N-k]: = (Rad * cos(Phase) + Rad * sin(Phase));
            A[k][N-j]: = (Rad*cos(Phase)-Rad * sin(Phase));
        END FOR
    END FOR
    InvFFT2D (A, X, N);
END
```